

Cite this: *Soft Matter*, 2015, 11, 368

Linear and non-linear wall friction of wet foams

Marie Le Merrer,^{†*a} Rémi Lespiat,^{‡b} Reinhard Höhler^{ab} and Sylvie Cohen-Addad^{*ab}

We study the wall slip of aqueous foams with a high liquid content. We use a set-up where, driven by buoyancy, a foam creeps along an inclined smooth solid wall which is immersed in the foaming solution. This configuration allows the force driving the bubble motion and the bubble confinement in the vicinity of the wall to be tuned independently. First, we consider bubble monolayers with small Bond number $Bo < 1$ and measure the relation between the friction force F and the bubble velocity V . For bubbles which are so small that they are almost spherical, the friction law $F \propto V$ is Stokes-like. The analysis shows that the minimal thickness of the lubricating contact between the bubble and the wall is governed by DLVO long-range forces. Our results are the first evidence of this predicted linear friction regime for creeping bubbles. Due to buoyancy, large bubbles flatten against the wall. In this case, dissipation arises because of viscous flow in the dynamic meniscus between the contact film and the spherical part of the bubble. It leads to a non-linear Bretherton-like friction law $F \propto V^{2/3}$, as expected for slipping bubbles with mobile liquid–gas interfaces. The Stokes-like friction dominates for capillary numbers Ca larger than the crossover value $Ca^* \sim Bo^{3/2}$. The overall friction force can be expressed as the sum of these two contributions. On this basis, we then study 3D foams close to the jamming transition with osmotic pressures Π small compared to the capillary pressure P_c . We measure the wall shear stress τ as a function of the capillary number, and we evidence two friction regimes that are consistent with those found for the monolayer. Similarly to this latter case, the total shear stress can be expressed as the sum of the Stokes-like friction term $\tau \propto Ca$ and the Bretherton-like one $\tau \propto Ca^{2/3}$. However, for a 3D foam, the crossover at a capillary number Ca^{**} between both regimes is governed by the ratio of the osmotic pressure to the capillary pressure, such that $Ca^{**} \sim (\Pi/P_c)^{3/2}$.

Received 15th July 2014
Accepted 23rd September 2014

DOI: 10.1039/c4sm01557f

www.rsc.org/softmatter

1 Introduction

An aqueous foam is a dense packing of gas bubbles in a soapy solution. This complex fluid exhibits a rich rheological behavior depending on gas volume fraction, bubble size and surfactant composition.^{1,2} For instance, for an applied shear stress larger than the yield stress, the foam flows as a shear-thinning fluid. The non-linear stress–strain rate relation observed in this regime is due to internal friction upon bubble rearrangements. It involves capillary interactions between neighboring bubbles, viscous friction in the liquid phase as well as interfacial dissipation.^{2,3} In general, the velocity of a simple liquid flowing near a solid smooth wall matches the wall velocity at the boundary. In contrast, a velocity mismatch is frequently observed in complex fluids such as foams, concentrated emulsions or soft

pastes.^{3–6} The wall slip phenomenon in 2D and 3D foams has been studied experimentally, numerically and theoretically mainly in the dry case (high gas volume fraction).^{7–13} It has been shown that the friction arises from the viscous flow in the films or in the liquid channels they form at their junctions — the so-called Plateau borders — in contact with the wall. Since the size of both the films and the Plateau borders strongly depend on the gas volume fraction, foam wall friction is expected to depend also on this parameter, or equivalently on the foam osmotic pressure which pushes the bubbles against each other and against the wall.^{14,15} With decreasing gas volume fraction, the osmotic pressure decreases and vanishes at the jamming transition. In this wet limit, the bubbles are quasi spherical with small contact films and thick Plateau borders. This geometry is very different from that of a dry foam where bubbles are polyhedral and Plateau borders slender, for which previous foam wall slip models have been developed. This raises the fundamental question: what are the mechanisms of friction at play in the wall slip of foams close to the jamming transition, and which are the laws that describe them? This issue is relevant for milli- and microfluidic devices^{16,17} and for many industrial applications¹⁸ where foams flow near solid boundaries, such as enhanced oil recovery, drilling operations or nuclear decontamination. In these applications, wall slip often needs to be

^aUniversité Paris 6, UMR 7588 CNRS-UPMC, INSP, 4 place Jussieu, 75005 Paris, France. E-mail: sylvie.cohen-addad@insp.upmc.fr

^bUniversité Paris-Est, LPMDI, 5 Bd Descartes, 77454 Marne-la-Vallée, France

[†] Present address: Institut Lumière Matière, UMR5306 Université Lyon 1-CNRS, Université de Lyon 69622 Villeurbanne cedex, France. E-mail: marie.le-merrer@univ-lyon1.fr

[‡] Present address: Saint-Gobain CREE, 550 avenue Alphonse Jauffret, BP20224, 84306 Cavaillon CEDEX, France.

enhanced to minimize pressure drops along the flow. In contrast, in rheological measurements, wall slip is a notorious artifact that needs to be minimized. Understanding its origin helps to achieve these goals.

The prediction of foam wall slip is a delicate problem due to the presence of surfactant molecules. As they adsorb on the liquid gas-interface and possibly on the wall surface, they have an impact on the van der Waals or electrostatic surface interactions, which set the static equilibrium contact film thickness. The interplay between surface forces and hydrodynamic forces determines the wall friction.^{19–21} In addition, surfactants can considerably affect the mechanical behavior of liquid–gas interfaces. It can be either mobile and tangential stress free as in a pure liquid, or rigid and able to sustain a tangential shear stress. The flow profile in the region between the bubble and the wall strongly depends on this stress boundary condition, and the mechanical dissipation increases with the interfacial rigidity.

In dry foams, it has been shown that, for mobile interfaces, the dissipation is dominated by the viscous flow in the dynamic meniscus between the film and the Plateau border.^{9,11} This mechanism is similar to the one encountered in the motion of a bubble pushed in a capillary tube, originally addressed by Bretherton,²² of a single soap lamella,²³ of trains of bubbles^{24,25} pushed in a narrow capillary, or of a flattened bubble creeping along a wall.^{26,27} Due to this mechanism, the wall shear stress scales as $V^{2/3}$ where V is the foam velocity at the wall. In contrast, for rigid interfaces,^{10,13} dissipation is dominated by the flow in the contact film, and this leads to different scalings of the wall shear stress with V .

In wet foams, where bubbles are quasi spherical, the dynamic meniscus vanishes and no longer contributes significantly to the viscous friction. A Stokes like friction scaling linearly with V is expected to contribute to the total drag, as observed in an emulsion⁶ or with isolated bubbles creeping along a solid wall.²⁶

The aim of this paper is to understand how wet foams slip along a solid smooth wall, depending on the bubble confinement. To tackle this question, we investigate bubble monolayers and 3D foams creeping along a slightly inclined plane immersed in a reservoir. This set-up allows the driving force as well as the confinement of the bubbles against the wall to be tuned independently. By studying the impact of these control parameters on the velocity of a bubble monolayer, we identify two friction mechanisms and the conditions under which one or the other dominates.

2 Previous wall friction models for a bubble or a dry foam

In this section we consider a bubble confined either in a monolayer or in a 3D foam that is pressed by buoyancy against a solid wall. We describe the size and the equilibrium thickness of the contact film. These parameters are determining for the wall friction for both monolayers and 3D foams since they set the area over which viscous friction occurs and the characteristic length where velocity gradients set in. We recall the existing

predictions for the viscous drag that accompanies the motion of an isolated bubble or of a dry foam sliding along a plane.

2.1 Sliding of an isolated bubble

We consider a gas bubble, of diameter d , which is immersed in an aqueous surfactant solution (surface tension γ , density ρ , and viscosity η). We describe the equilibrium shape of the bubble and recall the predictions of the drag force that it experiences when it slowly creeps along a plane slightly inclined with a small angle α with respect to the horizontal (Fig. 1a). The friction laws are summarized in Table 1.

Equilibrium bubble shape and film thickness. Under the action of the buoyancy component normal to the plane, the bubble is pressed against the wall. It is no longer spherical and flattens over a circular contact region, of diameter ℓ (Fig. 1a). We consider the case of total wetting of the surface by the solution so that a thin film remains between the flattened region and the wall. In addition, we consider bubbles that are small compared to the capillary length $a = \sqrt{\gamma/(\rho g)}$, *i.e.* small Bond numbers $\text{Bo} = (d/(2a))^2 < 1$. g denotes the magnitude of the gravity acceleration \mathbf{g} . In this regime, neglecting the small distortion of the spherical cap that is the outer shape of the bubble, the balance between the capillary force:

$$F_{\text{cap}} = \pi\gamma \frac{\ell^2}{d} \quad (1)$$

and the normal component of the buoyancy force exerted on a bubble:

$$F_{\text{b}} = (\pi/6)\rho g d^3 \cos \alpha \quad (2)$$

yields the diameter of the contact:^{20,26,28}

$$\ell = \sqrt{\frac{\cos \alpha}{6}} \frac{d^2}{a} \quad (3)$$

When the bubble is at rest ($\alpha = 0$), the thickness of the contact film is set by the balance between the capillary force and long range forces that tend to push the bubble away from the plane, due to both van der Waals and electrostatic repulsions (DLVO interactions). Since for $\text{Bo} \ll 1$, the bubble is only slightly deformed, we consider the interaction between a gas sphere and a solid plane separated by a distance h , with liquid between them. The van der Waals force acting on the bubble is then given by:²⁹

$$F_{\text{vw}}(h) = -\frac{A_{\text{eff}}d}{12h^2} \quad (4)$$

where the effective Hamaker constant A_{eff} depends on the Hamaker constants of the liquid and the solid phases, denoted A_{L} and A_{S} respectively: $A_{\text{eff}} \cong -\sqrt{A_{\text{L}}}(\sqrt{A_{\text{S}}} - \sqrt{A_{\text{L}}})$. Since $A_{\text{S}} > A_{\text{L}}$, we have $A_{\text{eff}} < 0$, and the effective van der Waals interaction is repulsive. Since the charged surfactant molecules adsorb either on the solid surface or on the liquid–gas interface, there is an additional electrostatic repulsion between the plane and the sphere. Its range is set by the Debye screening length κ_{D}^{-1} which depends on the electrolyte concentration c . The

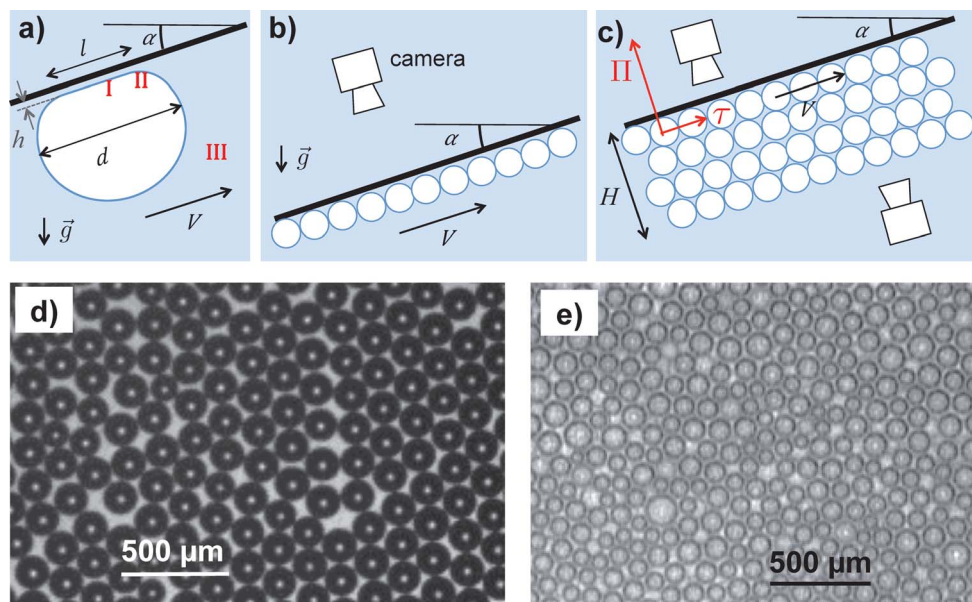


Fig. 1 Experimental configurations of: (a) a bubble, (b) a bubble monolayer, or (c) a 3D foam sliding along an inclined plane, with bubble diameter d smaller than the capillary length. (d) Snapshot of a bubble monolayer ($d = 170 \mu\text{m}$, 5% polydispersity). (e) Snapshot of the bubbles on top of a 3D foam ($d = 115 \mu\text{m}$, 10% polydispersity).

interaction potential energy, per unit surface area, between two planes separated by a distance h is, for a 1 : 1 electrolyte solution:²⁹

$$w(h) \approx 0.0482\sqrt{c} \tanh^2 \left[\frac{\Psi_o(\text{mV})}{103} \right] e^{-\kappa_D h} \quad (5)$$

Ψ_o is the surface potential expressed in mV and $w(h)$ is expressed in unit J m^{-2} . Using the Derjaguin approximation, the repulsive force between a sphere of diameter d and a plane, separated by h , is deduced from $w(h)$ as:²⁹

$$F_{\text{el}}(h) = \pi d w(h) \quad (6)$$

The force balance is then written as

$$F_{\text{vw}}(h) + F_{\text{el}}(h) = F_{\text{cap}} \quad (7)$$

The solution of eqn (7) using eqn (1) and (3)–(7) gives the equilibrium separation distance h_o , expected to be in the range 5–50 nm.

Friction force exerted on an isolated bubble. When the plane is tilted by an angle α , the bubble moves with a velocity V in the reference frame of the plane. In steady motion, the viscous drag force exerted on the bubble, denoted by F , is balanced by the tangential component of the driving buoyancy force:

$$F = (\pi/6)\rho g d^3 \sin \alpha \quad (8)$$

Dissipation of mechanical energy may arise from flow in the contact film (that we call region I, cf. Fig. 1a), in a dynamic rim (region II) that extends between the film and the part of the bubble which retains its static shape, or around the bubble further away from the wall (region III). In the absence of any surfactant, the liquid–gas interface is tangential stress free. However, the presence of surfactants has a strong impact on the stress boundary condition, which in turn affects the flow profiles in the three regions. Indeed, surfactant covered interfaces can offer resistance to shear or compression–dilation as described by surface stress constitutive laws.³¹ Two limiting

Table 1 Summary of friction laws for an isolated bubble creeping along an inclined plane, with the corresponding assumptions and regimes of validity

Boundary condition	Film thickness h_o fixed by disjoining pressure ^{20,30}	Film thickness fixed by hydrodynamics ^{13,27}	
	$\text{Bo} \ll 1$	$\text{Bo} \ll \alpha^2$	$\alpha^2 \ll \text{Bo} < 1$
Mobile (slipping)	$F = \pi\gamma d \text{Ca} \left(-\frac{3}{5} \ln[2h_o/d] + 1.71 \right)$	$F = \frac{6\pi}{5} \gamma d \text{Ca} \ln \left[\frac{\pi\rho g a d^2}{3F} \right]$	$F = 1.72\gamma \sqrt{\cos \alpha} \frac{d^2}{a} \text{Ca}^{2/3}$
Rigid (sliding)	$F = \pi\gamma d \text{Ca} \left(-\frac{8}{5} \ln[2h_o/d] + 2.86 \right)$	$F = \frac{8\pi}{5} \gamma d \text{Ca} \ln \left[\frac{\pi\rho g a d^2}{3F} \right]$	$F = 0.29\gamma \cos \alpha \frac{d^3}{a^2} \text{Ca}^{1/3}$
Rigid (rolling)	—	—	$F = 2.17\gamma \sqrt{\cos \alpha} \frac{d^2}{a} \text{Ca}^{2/3}$

cases can be distinguished: (i) in the mobile case, the interface is tangential stress free as it would be for a pure (clean) liquid. Then the bubble undergoes what is called a slipping motion along the plane. In practice this can also be achieved with high surfactant concentrations, well above the critical micellar concentration (cmc), that allow complete surface remobilization.^{32,33} (ii) In the rigid case, the interface can sustain a tangential shear stress and behaves as if it were incompressible and rigid, yet deformable (like a sheet of paper). When the liquid velocity at the interface is equal to the bubble velocity V , the bubble slides with a no-slip boundary condition. If the interfacial velocity is equal to that of the wall, then the bubble experiences a rolling motion.

Due to the liquid confinement near the wall, liquid velocity gradients set in, which induce viscous friction in region I. Therefore, the viscous drag is not given by a simple Stokes friction law ($F = 2\pi\eta Vd$ and $F = 3\pi\eta Vd$ for the mobile and rigid cases respectively³⁴) expected if the bubble were far away from the wall. Using a lubrication argument, the pressure drop between the front and the rear of a hard sphere can be calculated.^{20,27} The resulting tangential force is found to be linear in V to first order with a prefactor that depends logarithmically on the separation distance h between the bubble and the plane. Assuming that h is fixed by its static equilibrium value $h_o \ll d$ imposed by long range forces, the viscous drag (due to viscous friction in regions I and III — region II does not exist for hard spheres) has been predicted, to first order in h_o/d , in the mobile case:²⁰

$$F = \pi\eta Vd \left(-\frac{3}{5} \ln[2h_o/d] + 1.71 \right) \quad (9)$$

and in the rigid case, as the bubble slides:³⁰

$$F = \pi\eta Vd \left(-\frac{8}{5} \ln[2h_o/d] + 2.86 \right) \quad (10)$$

For very small bubbles, distortion from the spherical shape is negligible and eqn (9) and (10) are expected to predict their drag force. For bubbles that are slightly larger, so that the distortion of the bubble due to the action of the disjoining pressure over the contact region is more pronounced, there is a region that logarithmically matches the flat film to the spherical cap. The contribution of the viscous friction in this matching region to the total drag has also been predicted for bubbles with mobile interfaces.²⁰ We do not discuss further this prediction because it is not relevant for our experiments. It holds for bubble sizes such that $h_o^{1/3} a^{2/3} \ll d \ll a$ and for slow flow with a capillary number $Ca = \eta V/\gamma$ much smaller than $Ca_{\max} \cong 3.4(h_o/d)^{3/2}$. However, in this case as well as in the cases of undeformed bubbles (eqn (9) and (10)), for a given h_o or d , the drag force F is always Stokes-like in the sense that it increases linearly with the sliding velocity V .

At larger velocity, but still small capillary number $Ca \ll 1$, the thickness of the lubricating film is not equal to its static equilibrium value, but it is rather set by the flow in regions I or II. Hodges *et al.* have predicted the hydrodynamic film thickness as well as the bubble speed as a function of the force exerted on the bubble.²⁷ For tiny bubbles $Bo \ll \alpha^2$, regions I and II merge

and the bubble remains quasi-spherical. The separation distance is determined by the balance between the buoyancy component normal to the wall and the hydrodynamic lift force: h increases with the velocity or equivalently with the drag force. Thus, shear gradients in the confined region are reduced compared to the case of the fixed static equilibrium distance. The resulting drag force F deviates from the Stokes force²⁷ due to a logarithmic factor that slowly varies with V . In the mobile case (slipping motion), the following relation is predicted:²⁷

$$F = \frac{6\pi}{5} \eta Vd C(F) \quad (11)$$

The prefactor $C(F)$ decreases logarithmically with the drag force (or the velocity) as:

$$C(F) = \ln \left[\frac{\pi \rho g a d^2}{3F} \right] \quad (12)$$

In the rigid case for a sliding motion, the predicted drag force is:²⁷

$$F = \frac{8\pi}{5} \eta Vd C(F) \quad (13)$$

These implicit relations can be inverted numerically to deduce the force as a function of the velocity.

For larger bubbles $\alpha^2 \ll Bo < 1$, region II corresponds to a dynamic meniscus where the flat film of constant thickness h matches the spherical cap. In the dynamic meniscus, viscous flow is driven by capillary forces which act against the deformation of the liquid–gas interface. This problem is similar to the motion of a small bubble in a capillary tube filled with liquid, first studied by Bretherton for a bubble with mobile interfaces.²² Assuming a 2D geometry, the predicted drag force, per unit length of the dynamic meniscus, is $4.9\gamma Ca^{2/3}$.¹³ A recent computational analysis³⁵ has found a slightly smaller prefactor equal to 3.6. For a 3D bubble, since the length of region II scales as ℓ (eqn (3)), we expect the net drag force resulting from pressure drop difference between the front and the rear of the bubble to scale as $\gamma \ell Ca^{2/3}$ as previously derived using scaling arguments.²⁶ Hodges *et al.* have calculated the prefactor for a 3D bubble with mobile interfaces, and found:²⁷

$$F = 4.2\gamma \ell Ca^{2/3} \quad (14)$$

Combined with eqn (3), this gives:

$$F = 1.72\gamma \sqrt{\cos \alpha} \frac{d^2}{a} Ca^{2/3} \quad (15)$$

In the case of rigid interfaces with a rolling bubble motion, the same expression¹³ is predicted with a prefactor multiplied by $2^{1/3}$. For a sliding motion, the contact film (region I) is sheared and the dissipation is dominated by the viscous friction due to this Couette flow. The drag force is predicted to be a non-linear function of Ca , but with a smaller exponent than in the mobile case:²⁷

$$F = 0.29\gamma \cos \alpha \frac{d^3}{a^2} Ca^{1/3} \quad (16)$$

Finally, we note that as soon as the film thickness deviates from its static equilibrium value and is rather set by the hydrodynamic flow, the friction force becomes a non-linear function of the sliding velocity. In section 4.2 we will compare the predictions given by eqn (9), (10), (11), (13), (15) and (16) to our measurements of the force exerted on an isolated bubble, depending on its size and velocity, and we will discuss how the predictions compare to the drag force exerted on compact monolayers where bubbles get close to each other (Fig. 1d).

2.2 Sliding of a foam

We consider a slab of foam of thickness H containing several layers of bubbles of diameter $d \ll a$, immersed in a reservoir of surfactant solution, and which slowly creeps along an inclined plane (*cf.* Fig. 1c). We describe the equilibrium shape of a bubble in contact with the wall and we recall the existing predictions of shear stress exerted on the solid by a sliding dry foam.

Equilibrium shape of the bubbles in the layer in contact with the wall. These bubbles exert on the wall an upward force, resulting from the sum of the buoyant forces of all the bubbles below in the slab. Assuming an average gas volume fraction $\langle \Phi \rangle$ throughout the layer, of area A_0 , the force is written as: $\rho g \langle \Phi \rangle A_0 H$. Its component, per unit area, normal to the wall is, by definition, equal to the foam osmotic pressure Π at the wall.^{14,15,36} In consequence, bubbles flatten over an area of diameter ℓ , and similarly to the case of a single bubble, they remain separated from the wall by a thin film whose static equilibrium thickness is set by the balance between the long range forces (eqn (4)–(6)) and the capillary force F_{cap} given by:

$$F_{\text{cap}} = \frac{\pi}{4} \ell^2 P_c \quad (17)$$

where the capillary pressure P_c is the pressure difference between the gas and the liquid phases. Thus, the normal force, per unit area, exerted by the bubble layer in contact with the wall is related to the osmotic pressure by:

$$\Pi = \frac{4\Phi_s}{\pi d^2} F_{\text{cap}} \quad (18)$$

Φ_s is a dimensionless measure of the number of bubbles in contact with the wall, per unit surface: $\Phi_s = N\pi d^2/(4A_0)$ where N is the number of bubbles over a wall surface area A_0 . Eqn (17) and (18) show how the size of the contact film is set by the ratio of osmotic pressure to capillary pressure:

$$\ell = d \sqrt{\frac{\Pi}{\Phi_s P_c}} \quad (19)$$

The ratio Π/P_c represents the fraction of the wall area occupied by the contact films.^{14,37} Eqn (19) is the analog for 3D foams of eqn (3) that governs the film size in the individual bubble or monolayer cases. The variations of the osmotic pressure with the gas volume fraction Φ have been studied over a range that extends from the dry limit ($\Phi \rightarrow 1$) to packing fractions a few

percent above Φ_c , the packing fraction at the jamming transition:^{15,36}

$$\Pi = k \frac{\gamma(\Phi - \Phi_c)^2}{d\sqrt{1 - \Phi}} \quad (20)$$

$\Phi_c = 0.64$, $k = 6.4$ for disordered foams and $\Phi_c = 0.74$, $k = 14.6$ for ordered ones. This is consistent with the empirical expression previously proposed by Princen¹⁴ valid for disordered foams with $\Phi > 0.75$. Simulations show that at packing fractions no more than a few percent above Φ_c , Π scales as $(\Phi - \Phi_c)^{1.5}$ in the case of ordered foams^{15,38} and $(\Phi - \Phi_c)$ in the case of disordered foams.^{38,39} The vertical gas volume fraction profile in a foam layer, of thickness H , at static equilibrium in the gravity field can be deduced³⁶ from eqn (20). For instance, in a monodisperse ordered foam in contact with a liquid reservoir at the bottom, with a ratio $H/d = 15$, $d = 82 \mu\text{m}$ and the capillary length $a \approx 2 \text{ mm}$ as in our experiments, Φ increases from 0.74 at the bottom to 0.76 at the top.

Wall shear stress for a dry foam. The viscous friction between a dry 3D foam and a smooth wall has been predicted for both rigid or mobile liquid–gas interfaces.^{9,10,13} These models rely on the calculation of the friction F exerted on an isolated bubble creeping along the wall with a velocity V . Then, knowing the size of the contact film ℓ , this force is related to the macroscopic tangential stress exerted on the wall that we denote τ . This stress is a quantity that can be determined experimentally using rheological measurements. To relate F to τ , one needs to take into account the number of bubbles per unit wall area $4\Phi_s/(\pi d^2)$:

$$\tau = \frac{4\Phi_s F}{\pi d^2} \quad (21)$$

For the mobile case (free interface), Denkov *et al.* assume that the dissipation arises from the flow in the dynamic meniscus connecting the contact film to the Plateau border perpendicular to the wall. Thus, the force F scales with the capillary number according to the Bretherton–Hodges prediction eqn (15). The shear stress is further calculated assuming that the number of bubbles per unit area is $4/(\pi d^2)$. This approximation corresponds to $\Phi_s = 1$ and is thus only valid in the limit of a very dry foam. Again neglecting the liquid content between the bubbles, Denkov *et al.* relate the diameter of the film ℓ to the bubble size and to the gas volume fraction using eqn (19) with $\Phi_s = 1$ and the empirical relation formerly proposed by Princen¹⁴ in the range $0.75 < \Phi < 0.97$. They predict the wall shear stress in the limit of dry foams:⁹

$$\tau = C_1 \frac{\gamma}{d} \sqrt{\frac{\Pi}{P_c}} \text{Ca}^{2/3} \quad (22)$$

where C_1 is a constant prefactor. The wall shear stress exerted on a dry foam ($\Phi = 90\%$) has been measured for foams with different mean bubble sizes (d in the range 70 to 250 μm), liquid viscosities, and surface tensions.⁹ The variations of $\tau d/\gamma$ with Ca are found to be consistent with the prediction, eqn (22). Further experiments¹¹ have also confirmed the scaling with Ca and a first attempt to test the predicted dependency with the gas

volume fraction in the range $0.75 < \Phi < 0.95$ was made. However since eqn (22) is only valid for dry foams, the comparison between the data and this prediction is not pertinent for wet foams with $\Phi \lesssim 0.9$.

Note that, in the case of rigid interfaces, for sliding bubbles with a no-slip condition at the liquid–gas interfaces, the contact film is sheared which leads to additional dissipation of mechanical energy. Denkov *et al.* describe the flow of liquid in the film in analogy with the aquaplaning problem where a liquid film is entrained by the relative motion of a solid surface with respect to a fixed wall.^{9,10} According to this model, which holds in the dry limit, the shear stress can be decomposed as the sum of two contributions, one in $\text{Ca}^{1/2}$ due to the film, and a second one in Ca^δ ($\delta \approx 0.7$) due to the Plateau border. Recently, it has been pointed out that dissipation in the contact film can be taken into account in the framework of the Bretherton model.¹³ In the limit of dry foams, the shear stress is then predicted to be the sum of a $\text{Ca}^{1/3}$ term due to the film and to a $\text{Ca}^{2/3}$ due to the flow in the dynamics meniscus. The experiments^{9,11} show that both models can be fitted to the shear stress data. For a rolling bubble motion (*cf.* section 2.1), the wall shear stress is predicted by eqn (22) multiplied by a prefactor $2^{1/3}$ as previously shown.¹³

3 Experimental setup

The foaming solution is an aqueous solution, constituted of the surfactant tetradecyl trimethyl ammonium bromide (TTAB from Sigma, 99%, no. T4762) dissolved in pure water (Millipore milli-Q) at concentration $c = 9$ mM (0.3% g/g). This concentration is equal to twice the critical micelle concentration. The solution has viscosity $\eta = 0.94$ mPa s, surface tension $\gamma = 37.5$ mN m⁻¹ and density $\rho = 1.0$ g cm³ (*i.e.* capillary length $a = 1.95$ mm) at a temperature of 22.5 °C at which the wall slip experiments are performed. The liquid–gas interfaces have low interfacial rigidity with a dilational surface modulus of the order of a few mN m⁻¹ at low frequency.⁴⁰ Nitrogen bubbles are generated either using a flow focusing microfluidic device⁴¹ or by gas bubbling through a capillary tube (for the larger bubbles). Monodisperse monolayers are produced with a bubble diameter d chosen in the range 120 μm to 2.7 mm, with a polydispersity of about 5%. Polydispersity is defined as the normalized standard deviation of the bubble diameters. Monodisperse 3D foams are produced with $d = 82$ μm (polydispersity <3%). These foams are either used right after their production or let to age for a few minutes. In the former case, a polycrystalline foam structure is obtained. In the latter case, due to diffusive gas transfer between neighbours, the bubbles coarsen and the foam becomes polydisperse and disordered. After 10 min the average bubble size is $d = 115$ μm with 10% polydispersity. We use such foams as polydisperse samples.

We use an immersed inclined plane set-up similar to that previously used to probe the rheology of wet foams close to the jamming transition.⁴² The plane is constituted by the surface of a smooth plexiglass plate (15 mm \times 100 mm) that is maintained at an angle α with respect to the horizontal. α can be adjusted between 0.18° and 24° with a precision of 0.06°. The reservoir in

which the inclined plane is immersed is filled with the foaming solution. We collect bubbles in the reservoir at the bottom of the plane, and store them with a gate. Then the gate is opened and the bubbles are released. By controlling the gate opening we form either isolated bubbles, a bubble monolayer or a 3D foam that creep upward along the plane under the action of buoyancy. For the monolayer, the bubble motion is observed using a camera placed above the plane (Fig. 1b) while for the 3D foam we use two cameras (Fig. 1c), one above that records the motion of the bubbles in contact with the wall and a second one below that monitors the bubble motion at the bottom surface of the foam. If there is a difference between the top and the bottom velocities, the foam undergoes a shear flow that may lead to a dynamic dilatancy^{43,44} such that the gas volume fraction decreases compared to the static case. This second camera is also used to measure the foam thickness H with a laser light sheet at grazing incidence (not shown in Fig. 1c), as described in ref. 42. In our experiments, H ranges between 0.3 and 3 mm, which corresponds to about 3 to 30 bubble layers. Using either image correlations or tracking of packing vacancies, we measure the bubble velocity. We have checked that, in our experimental configuration, at a distance of more than 1 mm from the sidewalls, the velocity is constant and stationary.⁴² We use the top view images to measure the area fraction of the wall occupied by the bubbles, Φ_s . For all of the studied foams, we have $\Phi_s \approx 0.8$. For polydisperse foams, the average gas volume fraction $\langle \Phi \rangle$ in the foam layer is determined by a conductivity measurement using two electrodes flush-mounted in the plane⁴² (not shown in Fig. 1c). $\langle \Phi \rangle$ ranges between 0.58 ± 0.01 and 0.63 ± 0.01 . The values inferior to Φ_c reflect the shear induced dilatancy.⁴⁴ For monodisperse foams, a calculation assuming a perfectly ordered static structure (as in section 2.2), yields for our experimental parameters, average gas volume fractions $\langle \Phi \rangle$ in the range 0.750–0.763. We detect velocity differences between the bubbles at the top and at the bottom of the sample to be so small that we neglect the dilatancy effect. Since the foam structure is polycrystalline, we expect grain boundaries to reduce the gas volume fraction slightly, and we finally assume $\langle \Phi \rangle \approx \Phi_c = 0.74$.

4 Bubble monolayers

4.1 Results

Fig. 2 shows the velocity V measured for a bubble monolayer as a function of the sine of the tilt angle α , for bubble diameters ranging between $d = 120$ μm and $d = 2.7$ mm. The corresponding ranges of investigated Bond and capillary numbers are specified in Table 2. The driving force F exerted on a bubble is given by eqn (8). Thus the observed increase of V with both $\sin \alpha$ and d is consistent with eqn (8). In the steady regime, F is equal to the drag force exerted on a bubble. Fig. 3 shows the variations of the drag force with the velocity obtained for each bubble size, for the same data as in Fig. 2. In this logarithmic plot, we observe two regimes, depending on the bubble size: For small bubbles ($d \leq 290$ μm , Fig. 3b), we have a linear relationship $F \propto V$, while for large bubbles ($d \geq 950$ μm , Fig. 3c), F varies sub-linearly with the velocity as $F \propto V^{2/3}$. For intermediate

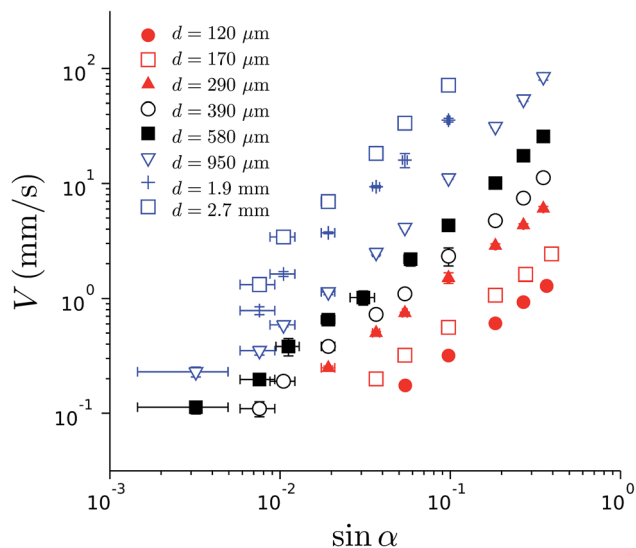


Fig. 2 Bubble velocity V in a dense monolayer as a function of $\sin \alpha$, for different bubble diameters d as labelled, with Bo numbers given in Table 2.

Table 2 Bubble diameters and velocities, with corresponding Bond and capillary numbers for the experiments with bubble monolayers. The capillary number Ca^* corresponding to the crossover between linear and non-linear friction regimes for a dense monolayer is calculated using eqn (24) with $A = 15.5$ and $B = 3.2$. The capillary length is equal to $a = 1.95$ mm

d (μm)	Bo	V (mm s^{-1})	Ca	Ca^*
120	0.0009	0.17–1.3	4×10^{-6} to 3×10^{-5}	2×10^{-6}
170	0.002	0.20–2.5	5×10^{-6} to 6×10^{-5}	6×10^{-6}
290	0.005	0.25–6.2	6×10^{-6} to 2×10^{-4}	3×10^{-5}
390	0.01	0.10–11	3×10^{-6} to 3×10^{-4}	7×10^{-5}
580	0.02	0.11–27	3×10^{-6} to 7×10^{-4}	2×10^{-4}
950	0.06	0.22–85	6×10^{-6} to 2×10^{-3}	1×10^{-3}
1900	0.2	0.77–36	2×10^{-5} to 9×10^{-4}	8×10^{-3}
2700	0.5	1.1–73	3×10^{-5} to 2×10^{-3}	2×10^{-2}

bubble sizes, the exponent of the power law varies progressively from 1 to $2/3$.

4.2 Discussion

Small bubbles. The linear regime $F \propto V$ observed with the small bubbles ($Bo \leq 0.005$) is consistent with the linear friction observed for an emulsion ($\Phi = 0.75$) sliding along a non-adhering smooth plane.⁶ In section 2.1, we have recalled the existing predictions for the drag force exerted on an isolated bubble where friction arises not only in the contact film but also around the spherical cap (region III). On the one hand, White and Carnie²⁰ have predicted the Stokes-like friction when the separation distance h in the contact region is constant and equal to its static equilibrium value h_0 (eqn (9) or (10)). On the other hand, Hodges *et al.*²⁷ have calculated the drag force when

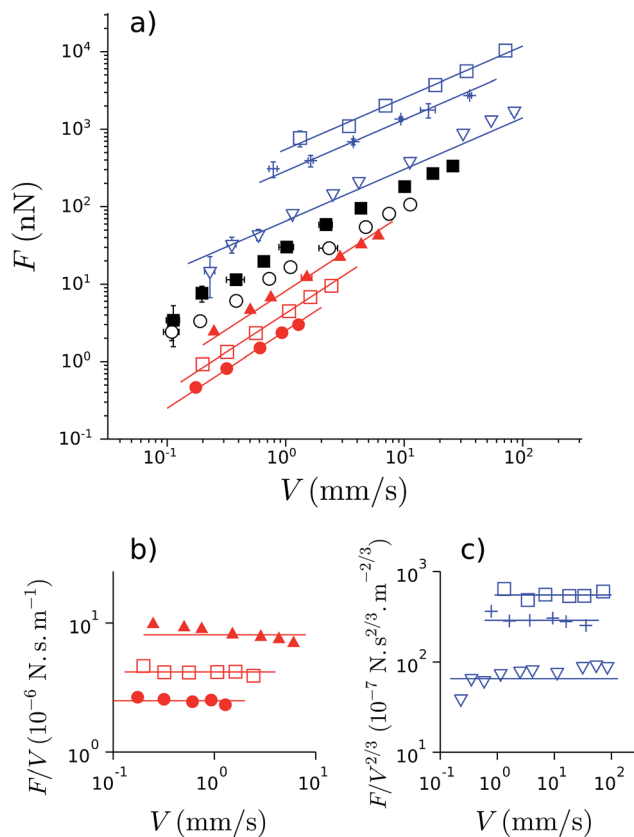


Fig. 3 Dense bubble monolayer: (a) friction force F measured as a function of the velocity V , for different bubble diameters d (same data with same symbols as in Fig. 2). The lines indicate power laws fitted to the data: $F \propto V^{2/3}$ (blue lines) and $F \propto V$ (red lines). (b) The quantity F/V is plotted as a function of V for the small bubbles and (c) the quantity $F/V^{2/3}$ is plotted as a function of V for the large bubbles.

the distance is set by viscous forces (eqn (11) or (13)). Compared to these predictions for isolated bubbles, we expect the viscous friction in region III to be reduced in the case of monolayers where neighboring bubbles move at the same speed. Furthermore the surface stress condition is not entirely known in our experiments: in view of the composition of the foaming solution, we expect that the interfaces do not perfectly behave as free surfaces, but rather exhibit small residual surface stress due to incomplete remobilization of the interfaces.

Thus to determine which mechanism sets the separation distance and to delineate the impact of the friction between neighboring bubbles from that of the interfacial mobility, we have measured the velocity of isolated small bubbles in the linear Stokes-like regime. We consider bubbles dispersed in a diluted monolayer where the fraction of the wall area occupied by the bubbles Φ_s is small. In Fig. 4, we compare our data obtained for the bubble diameter $d = 290$ μm to the different predictions. We observe that eqn (11) and (13), corresponding to a separation distance set by the flow, strongly underestimate the observed drag force, for both mobile and rigid boundary condition assumptions. This suggests that the actual separation distance is much smaller than the one predicted by this model. Similar results are obtained with the smaller bubbles ($d = 120$ μm

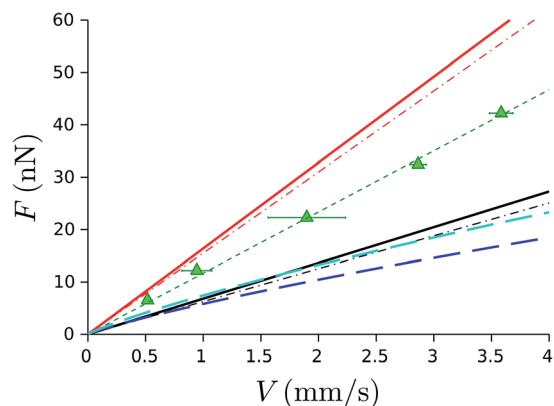


Fig. 4 Drag force F measured on an isolated bubble, with a diameter $d = 290 \mu\text{m}$, in a diluted monolayer (with surface fraction Φ_s in the range 8–33%), as a function of the creeping velocity V . The green symbols correspond to the data points. The black and red lines represent the force predicted when the separation distance is fixed by long range forces, with (i) mobile interfacial condition (eqn (9)) and $\Psi_o = 50 \text{ mV}$ (thick solid black) or $\Psi_o = 200 \text{ mV}$ (dot-dashed black), or (ii) rigid interfacial condition (eqn (10)) and $\Psi_o = 50 \text{ mV}$ (thick solid red) or $\Psi_o = 200 \text{ mV}$ (dot-dashed red). The thick dashed blue lines show the drag force when the separation distance is set by the viscous flow, with mobile interfacial condition (eqn (11)) (dark blue) and rigid interfacial condition (eqn (13)) (light blue). The dashed green line illustrates the equation: $F = 11.7 V$ with F in nN and V in mm s^{-1} .

and $d = 170 \mu\text{m}$). We conclude that our results are incompatible with the models eqn (11) and (13) where the separation distance is set by hydrodynamic forces.

As illustrated in Fig. 5 for the three smallest bubble diameters, we find that the friction force varies linearly with the slipping velocity such that $F = \zeta_b V$, and that the friction coefficient ζ_b increases with the bubble size (cf. Table 3). To analyze this friction law further, the static separation distance h_o is required. For the surfactant solution used here, we have:²⁹ $A_{\text{eff}} \approx -1 \times 10^{-20} \text{ J}$ and Ψ_o in the range 50–200 mV. For our surfactant concentration, $\kappa_D^{-1} = 3.2 \text{ nm}$. Solving eqn (7) with these parameters, we estimate the equilibrium distances $h_o \approx 11\text{--}16 \text{ nm}$ for $d = 120 \mu\text{m}$, $h_o \approx 9\text{--}13 \text{ nm}$ for $d = 170 \mu\text{m}$, and $h_o \approx 6\text{--}10 \text{ nm}$ for $d = 290 \mu\text{m}$. Consequently, with these equilibrium thicknesses, we can estimate the theoretical coefficients expected in the limit of mobile interfaces using eqn (9) or in the limit of rigid interfaces using eqn (10). The calculation shows that for a given bubble size d , ζ_b does not vary significantly in the range of expected thicknesses h_o and potentials Ψ_o , both in the mobile and in the rigid cases, as can be seen in Fig. 4. The predicted ζ_b are given in Table 3. We conclude that, for each bubble size, the measured coefficient falls within the expected range given by the mobile and rigid limit values. This is consistent with previous measurements on small bubbles sliding along a plane in a salty solution, which showed that the terminal velocity is affected by the disjoining pressure.²¹

Thus, from the analysis of the isolated bubble data, we conclude that the separation distance is set by DLVO forces and that the interface rigidity is intermediate between a completely mobile (free surface) and an entirely rigid one (no slip boundary condition), and we consistently expect this behavior to affect the

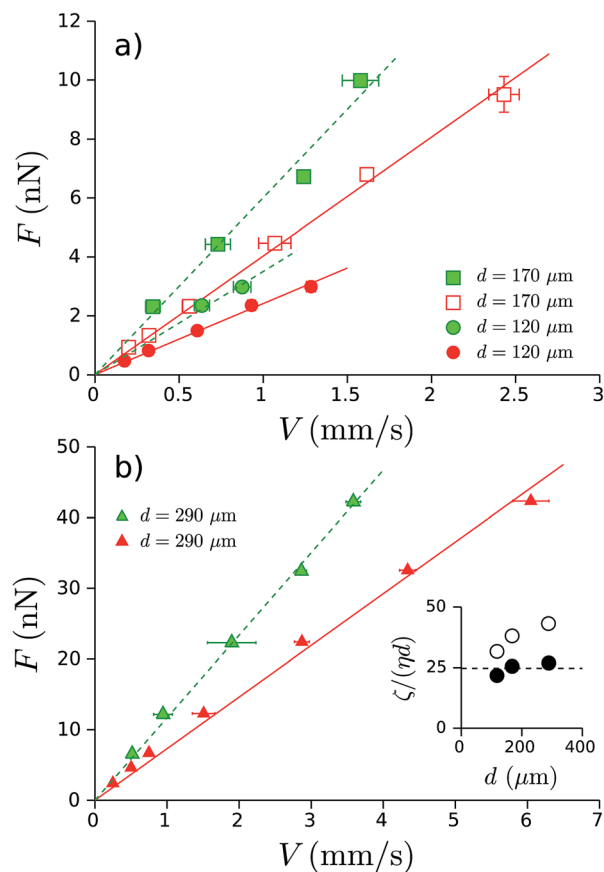


Fig. 5 Monolayer friction in the linear regime: force F exerted on a bubble in a dense monolayer vs. creep velocity (red symbols, the data are the same as those of Fig. 2) compared to the force F exerted on an isolated bubble, in a diluted monolayer (with surface fraction Φ_s in the range 2–33%) (green symbols), for different bubble sizes as labelled in (a) and (b). The lines represent linear regressions: $F = \zeta_b V$ in the dilute regime (dotted lines) and $F = \zeta_m V$ for the monolayer (solid lines). The values of the coefficients are reported in Table 3. In (b), the inset shows the variation of the friction coefficient with bubble size measured for the individual bubble (\circ), and for the dense monolayer (\bullet). The dashed line corresponds to the average monolayer value $\zeta_m = 25\eta d$.

friction of the monolayer. As can be seen in Fig. 5, for a given bubble size, the friction exerted on a monolayer is systematically less than the friction exerted on an isolated bubble. This result indicates that dissipation around the spherical cap (region III) is more pronounced for an individual bubble than it

Table 3 Values of the bubble friction coefficients measured in a diluted monolayer, ζ_b , or in a dense monolayer, ζ_m , and predicted coefficients for a single bubble either with mobile interfaces $\zeta_b^{\text{mobile}} = F/V$ (eqn (9)) or rigid interfaces $\zeta_b^{\text{rigid}} = F/V$ (eqn (10)) for the estimated equilibrium thicknesses (see text)

$d (\mu\text{m})$	120	170	290
$\zeta_b (10^{-6} \text{ N s m}^{-1})$	3.5	6.0	11.7
$\zeta_b^{\text{mobile}} (10^{-6} \text{ N s m}^{-1})$	2.4	3.6	6.5
$\zeta_b^{\text{rigid}} (10^{-6} \text{ N s m}^{-1})$	5.8	8.6	15.9
$\zeta_m (10^{-6} \text{ N s m}^{-1})$	2.4	4.0	7.3

is for a bubble inside a dense monolayer. This is also consistent with the fact that in a monolayer, there is no dissipation in the interstices in between neighboring bubbles, and that only friction with the lower part of the spherical cap at the interface with the liquid reservoir may remain. From the linear variations shown in Fig. 5, we deduce the friction coefficient of the monolayer $\zeta_m = F/V$. Whereas $\zeta_b/(\eta d)$ increases by about 30% with the bubble size, the increase of $\zeta_m/(\eta d)$ is less pronounced as shown in the inset of Fig. 5. In the following analysis, we will take the average value $\zeta_m/(\eta d) = 25$.

Large bubbles. We now turn to large bubbles *i.e.* with Bond numbers $Bo \geq 0.06$ where we observe a power law variation of the friction force, $F \propto V^{2/3}$. It extends over at least two decades in velocity (*cf.* Fig. 3 and Table 2) where the predictions based on the lubrication hypothesis hold.^{22,27} This scaling is consistent with previous experimental results on relatively dry foams ($\Phi \geq 0.90$), with mobile interfaces, sliding along a plane.^{9,11} According to eqn (15), we expect the force exerted on one bubble to scale as $\gamma(d^2/a)\sqrt{\cos \alpha}Ca^{2/3}$. Thus, we plot in Fig. 6 the force as a function of this quantity. We observe a very good collapse of the data on a master curve. By performing least square regression based on the percentage error (relative to the observed value, with a level of confidence of 95% and equal weight to each data point), we find a prefactor equal to 4.6 ± 0.5 . This prefactor is about 2.5 times larger than the prefactor expected for an isolated bubble with a tangential stress free boundary condition (eqn (15)). A similarly large prefactor was observed in the friction of a soap lamella sliding in a tube, but it was not elucidated.²³ In this 2D geometry, Dollet *et al.* measured the viscous force per unit length $F_{2d} \approx 13\gamma Ca^{2/3}$ for $5 \times 10^{-3} < Ca < 10^{-1}$, to be compared to theoretical predictions $F_{2d} \approx 5\gamma Ca^{2/3}$ for mobile interfaces.^{22,23,27}

In the presence of surfactants, instantaneous surface stresses due to surface stretching can build up and rigidify the interfaces. In the Landau–Levich coating problem as well as in

the Bretherton bubble problem, this leads to a thicker entrained film and a larger friction force compared to the free surface case.^{13,45,46} For soluble surfactants, surface stresses fade away due to surfactant surface diffusion or convection, and due to adsorption from the liquid beneath. If these processes are fast compared to the characteristic time scale of the surface stretching, the interface is remobilized and behaves as a free one. In contrast, if they are too slow, the interface becomes rigid and two sub-cases can be distinguished as recalled in section 2.1: (i) if the bubble slides with a no-slip boundary condition, the force is expected to vary as $Ca^{1/3}$ as given by eqn (16). Such a behavior is not observed for our monolayers as shown in Fig. 6. (ii) If the interface undergoes a rolling motion, the friction force is expected to scale as $Ca^{2/3}$ and it is increased by a factor $2^{1/3}$ compared to the free surface case¹³ (eqn (15)). Since we observe a $Ca^{2/3}$ scaling and an enhanced prefactor with our monolayers made of large bubbles, we now check whether surface remobilization can be achieved in the range of investigated Ca .

Following the previously proposed arguments^{32,33} for surface remobilization, a first condition is that the film acts as a surfactant reservoir to replenish the surface. This capacity is measured by the parameter $\sigma = \Gamma_o/(ch)$ where h is the entrained film thickness and Γ_o is the equilibrium surfactant surface concentration. For the bubble problem, h is fixed by the bubble diameter: $h \approx dCa^{2/3}$, thus $\sigma \approx \Gamma_o/(cdCa^{2/3})$. The condition is written as:³² $\sigma \ll 0.01$. Here, the maximum value of Ca is 2.5×10^{-3} , and for $d = 950 \mu\text{m}$ we have $\sigma \approx 0.02$. Thus this first condition is not satisfied. A second condition is that the time τ_a for surfactants to adsorb on the interface to restore the equilibrium concentration Γ_o should be short enough compared to the time scale of surface stretching $\tau_s \approx \ell_r/V$ where ℓ_r is the length of the dynamic meniscus. This condition is written as:³² $\tau_a/\tau_s \approx \lambda/d \ll 1$, where $\lambda = (\gamma_o - \gamma)\Gamma_o/(k\eta)$, γ_o being the surface tension of pure water and k the rate of adsorption. For our TTAB solution, we have: $c = 9 \text{ mM}$, $k \approx 10^{-3} \text{ ms}^{-1}$, $\Gamma_o \approx 3 \times 10^{-6} \text{ mol m}^{-2}$, thus $\lambda \approx 0.01 \text{ m}$, which yields $\lambda/d \approx 4$. Thus this second condition is not satisfied either. Although the surfactant concentration is above the cmc, it is not large enough to achieve complete surface remobilization. Consequently, we expect instantaneous surface tension gradients to set in. Since $\lambda/d > 1$, we can estimate their effect as if the surfactant were insoluble on the time scale of the flow in the dynamic rim. Following Park,⁴⁵ we introduce the Marangoni number $M = -(I_o/\gamma)(\partial\gamma/\partial\Gamma)_{\Gamma_o}$, and we estimate it as: $M \approx (\gamma_o - \gamma)/\gamma_o \approx 0.5$. For this M value and the investigated range $10^{-5} < Ca < 10^{-3}$, the maximum of the reinforcement factor is expected.⁴⁵ However a factor of $2^{1/3} \approx 1.3$ on the drag force will give a prefactor of 2.2 in eqn (15) which remains smaller than the observed one (4.6). This difference remains to be elucidated as in a previous study.²³ A possible reason may be that the extension of the film (region I) is not long enough for the asymptotic regime assumed in the Landau–Levich–Bretherton model to be reached.

Drag force exerted on a bubble monolayer for an extended range of Bond numbers. We observe in Fig. 3 that, for bubbles with intermediate Bond numbers ($0.005 < Bo < 0.06$), the friction force increases with V following a power law with an exponent comprised between $2/3$ and 1 . Such a non-linear

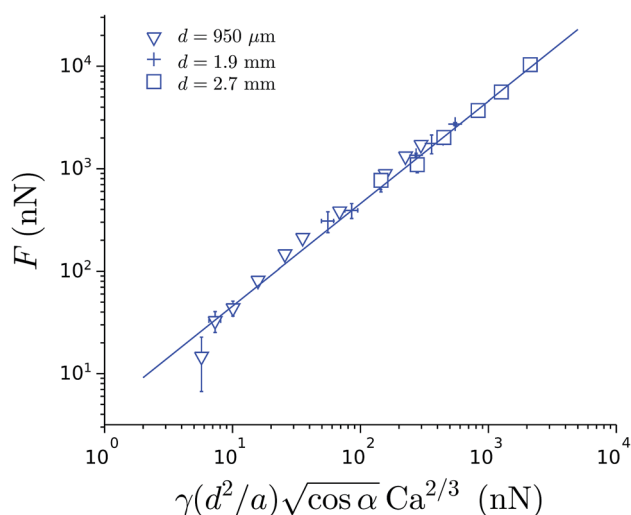


Fig. 6 Dense bubble monolayer: friction force F exerted on a bubble for $d \geq 950 \mu\text{m}$ (same data as in Fig. 2). The straight line corresponds to $F = 4.6\gamma(d^2/a)\sqrt{\cos \alpha}Ca^{2/3}$.

friction law has been previously evidenced for isolated bubbles slipping along an inclined plane immersed in an oil reservoir,²⁶ for $0.01 < \text{Bo} < 1$. The friction was attributed to dissipation in the dynamic rim (region II) and to a Stokes-like friction (regions I and III) with a friction coefficient independent of the film thickness. Using scaling arguments, the total drag was predicted to be the sum of a force $F \sim \gamma d \text{Ca}$ and of a Bretherton-like force $F \sim \gamma \ell \text{Ca}^{2/3} \sim \gamma (d^2/a) \text{Ca}^{2/3}$, the latter being consistent with the (more recent) prediction given by eqn (15) for mobile interfaces. For the bubble monolayer, ℓ is given by eqn (3). Thus, following this line of thought, we expect the drag force exerted on a bubble in a dense monolayer to be the sum of two terms scaling with Ca and $\text{Ca}^{2/3}$ respectively:

$$F = A\gamma d \text{Ca} + B\gamma (d^2/a) \sqrt{\cos \alpha} \text{Ca}^{2/3} \quad (23)$$

A least square regression based on the percentage error, with 95% level of confidence taking into account the whole set of data of Fig. 3 yields: $A = 15.5 \pm 2.9$ and $B = 3.2 \pm 0.4$. In Fig. 7 we plot the measured force F data as a function of the quantity $A\gamma d \text{Ca} + B\gamma (d^2/a) \sqrt{\cos \alpha} \text{Ca}^{2/3}$ with these fitted values of A and B . We observe a good collapse of the data on a master curve that supports the interpretation of the total dissipation as the sum of the Stokes- and Bretherton-like forces. It is also consistent that the fitted parameters are of the same order of magnitude as the parameters deduced from the analysis of the asymptotic regimes of small and large bubbles that correspond to: $A = \zeta_m/(\eta d) = 25$ and $B = 4.6$. We see in Fig. 7 that a simple addition of the forces using these parameters shifts the data towards larger abscissae which means that it leads to a slight overestimation of the actual drag force exerted on the monolayer.

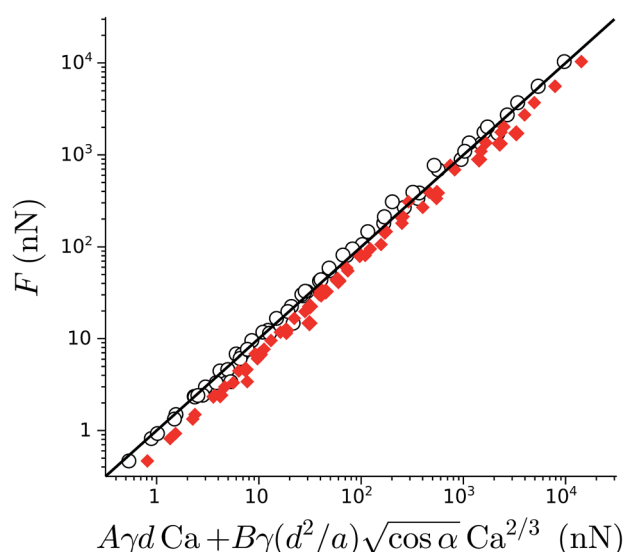


Fig. 7 Dense bubble monolayer: measured friction force F as a function of $A\gamma d \text{Ca} + B\gamma (d^2/a) \sqrt{\cos \alpha} \text{Ca}^{2/3}$ for the whole ensemble of data shown in Fig. 3 for two sets of parameters: fitted values $A = 15.5$ and $B = 3.2$ (empty circles), values deduced in the limits of small bubbles (Fig. 5, $A = 25$) and large bubbles (Fig. 6, and $B = 4.6$) (red diamonds). The straight line shows the merit of the fit: it illustrates the equation $F = X$ where X denotes the abscissa.

Finally we discuss the crossover from the linear to the non-linear friction regime. According to Hodges *et al.*²⁷ it should occur when the length of the dynamic meniscus which scales as $d \text{Ca}^{1/3}$, becomes comparable to the size of the film $\ell \sim d^2/a$ (we neglect here the weak dependency of ℓ upon the tilt angle α). This corresponds to $\text{Ca}^* \sim (d/a)^3$. Consistently, we can estimate the crossover by comparing the magnitude of both terms of eqn (23). The linear term will dominate for small bubbles or large velocities, such that:

$$\text{Ca} \gg \text{Ca}^* \equiv \left(\frac{2B}{A}\right)^3 \text{Bo}^{3/2} \quad (24)$$

With the fitted values $A = 15.5$ and $B = 3.2$ for the monolayer, we expect the crossover $\text{Ca}^* \approx 0.07 \text{Bo}^{3/2}$. Inspection of Table 2 shows that: (i) for the two smallest bubble size ($\text{Bo} = 0.0009$ and $\text{Bo} = 0.002$), we have $\text{Ca} \geq \text{Ca}^*$, (ii) for the two largest bubbles ($\text{Bo} = 0.2$ and $\text{Bo} = 0.52$), $\text{Ca} < \text{Ca}^*$, (iii) whereas for intermediate bubble sizes, Ca^* falls in the range of investigated Ca . This means that in the limit of small bubbles, the investigated range of Ca may not be extended enough to deduce a robust value of ζ_m without any residual contribution of the Bretherton-like force eqn (15). This may partly explain why the coefficient $A = 25$ deduced from the analysis of the dense monolayer in the range $\text{Bo} \ll 0.005$ is slightly larger than the coefficient resulting from the fit over the whole set of Bo data.

5 3D foams

5.1 Results

As a foam layer of thickness H and average gas volume fraction $\langle \Phi \rangle$ creeps along a plane tilted by an angle α with respect to the horizontal, the osmotic pressure Π at the wall is given by (cf. section 2.2):

$$\Pi = \rho g \langle \Phi \rangle H \cos \alpha \quad (25)$$

and the wall tangential shear stress τ by:

$$\tau = \rho g \langle \Phi \rangle H \sin \alpha \quad (26)$$

Π and τ are deduced from these equations using the values of H and $\langle \Phi \rangle$ as determined in section 3, for different imposed angles α . In Fig. 8, we plot for the smallest bubble size, the foam slipping velocity V measured as a function of the thickness H . We observe that, for a given inclination angle, we have $V \propto H$. According to eqn (26), this indicates that in this regime the shear stress τ is proportional to the velocity. This scaling is similar to the one that we observe for the Stokes-like friction of bubble monolayers in the range $\text{Bo} \leq 0.005$ (cf. Fig. 5 and Table 2). Furthermore, it is similar to that observed in moderately concentrated emulsions ($\Phi = 0.75$) slipping along a smooth repulsive wall.⁶ However no quantitative interpretation of the friction coefficient was given. The linear scaling that we observe differs qualitatively from the predicted (eqn (22)) and observed scalings for dry foams⁹ recalled in section 2.2.

We now study the variations of the wall shear stress τ versus V for foams close to the jamming transition, and for two different

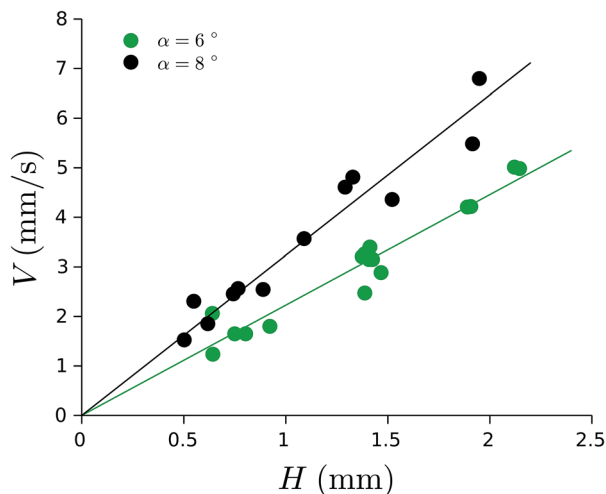


Fig. 8 Foam layer: slipping velocity V as a function of the foam thickness H for two inclination angles as labelled. The bubble diameter is $d = 82 \mu\text{m}$. Each straight line corresponds to a linear fit to the data with respective coefficients: 2.2 s^{-1} and 3.2 s^{-1} .

bubble sizes. The corresponding ranges of the capillary number and reduced osmotic pressure $\Pi d/\gamma$ are given in Table 4. As seen in Fig. 9a, for the small bubbles, data corresponding to different reduced osmotic pressures collapse on a linear master plot. However, for the large bubbles, the data do no longer collapse onto a linear plot, suggesting that a mechanism other than the Stokes-like friction is at play.

5.2 Discussion

To compare the friction coefficient of the 3D foam to that obtained for the bubble monolayer, we first relate the shear stress τ to the Stokes-like friction force $F = \zeta_m V$ exerted on a single bubble in a monolayer using eqn (21):

$$\tau = \frac{4\Phi_s}{\pi d^2} \zeta_m V \quad (27)$$

Similarly to the monolayer case, we can estimate the equilibrium separation distance from the balance between the long range forces and the capillary force using eqn (7) and (18), in the investigated range of osmotic pressure, and then calculate the corresponding coefficient $\zeta_b/(\eta d)$ that we would have for an isolated bubble in the mobile case using eqn (9): We estimate $\zeta_b/(\eta d) \approx 22$ which is very close to the value predicted for an isolated bubble with $d = 120 \mu\text{m}$ (cf. Table 3). For the parameters $\Phi_s = 0.8$, $d = 82 \mu\text{m}$, and using the value found for the monolayer $\zeta_m \approx 25\eta d$ (cf. Fig. 5), we expect the relation: $\tau \approx$

Table 4 Bubble diameters, reduced osmotic pressures and capillary numbers for the experiments with 3D foams

$d \text{ (}\mu\text{m)}$	$\Pi d/\gamma$	Ca	$\text{Ca}/(\Pi d/\gamma)$
82	0.006–0.04	3×10^{-5} to 2×10^{-4}	0.02–0.07
115	0.006–0.06	3×10^{-5} to 2×10^{-4}	0.006–0.3

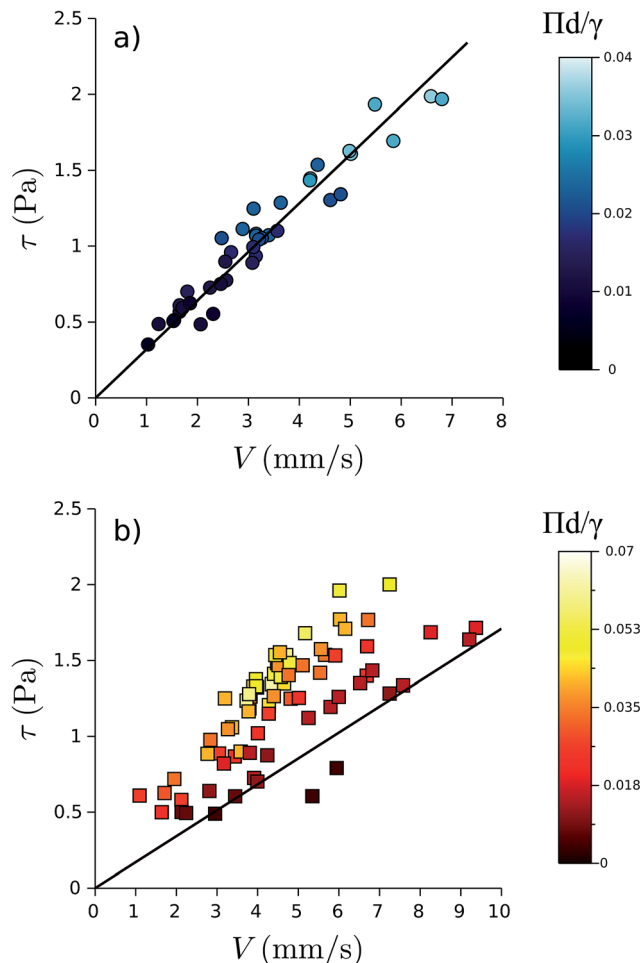


Fig. 9 Wall shear stress τ as a function of V for 3D foams, for different reduced osmotic pressures $\Pi d/\gamma$ as color-coded, with: (a) $d = 82 \mu\text{m}$. The straight line corresponds to a linear fit to the data with the fitted coefficient equal to $0.32 \pm 0.02 \text{ Pa s mm}^{-1}$. (b) $d = 115 \mu\text{m}$. The straight line has a slope equal to $0.17 \text{ Pa s mm}^{-1}$ as expected for a monolayer of the same bubble size (see text). For both foams, $\Phi_s = 0.8$.

$0.29V$ (with V in mm s^{-1} and τ in Pa) which is very close to the linear fit $\tau \approx 0.32V$ shown in Fig. 9a. For the larger bubbles (Fig. 9b), the wall friction is much larger than we would expect for a monolayer with the same bubble size. For the sake of comparison, the straight line in Fig. 9b represents eqn (27) with $\zeta_m = 2.4 \times 10^{-6} \text{ N s m}^{-1}$ (cf. Table 3).

By analogy with the friction of the monolayer, we assume that, in addition to the Stokes-like friction, there is also a contribution to the total friction arising from the flow in the dynamic menisci connecting the contact films to the Plateau borders. In the 3D foam, the diameter of the film is set by the ratio of osmotic pressure to capillary pressure (eqn (19)). Thus, using eqn (21) and (23), we expect a general expression for the shear stress exerted on the foam of the form:

$$\tau = \frac{4\Phi_s\gamma}{\pi d} \left(A\text{Ca} + B\sqrt{\frac{6\Pi}{\Phi_s P_c}} \text{Ca}^{2/3} \right) \quad (28)$$

This relation is consistent with the previous prediction of wall shear stress for dry foams with mobile interfaces (eqn (22)).

Here we consider the limit of extremely wet foams, where the bubbles are quasi spherical. In this limit, the capillary pressure is simply given by:

$$P_c \approx \frac{4\gamma}{d} \quad (29)$$

which yields the size of the contact film using eqn (19):

$$\ell = \frac{d}{2} \sqrt{\frac{\Pi d}{\gamma \Phi_s}} \quad (30)$$

Inserting this expression for ℓ into the eqn (28) gives the following prediction:

$$\tau = \frac{4\Phi_s\gamma}{\pi d} \left(A Ca + B \sqrt{\frac{3\Pi d}{2\Phi_s\gamma}} Ca^{2/3} \right) \quad (31)$$

where the coefficients A and B are assumed to be the same as for the bubble monolayer. By comparing both terms of eqn (31), we expect the linear Stokes-like friction to dominate the wall shear stress when $Ca \gg Ca^{**}$ where:

$$Ca^{**} \equiv \left(\frac{B}{A} \right)^3 \left(\frac{6\Pi}{\Phi_s P_c} \right)^{3/2} \approx \left(\frac{B}{A} \right)^3 \left(\frac{3\Pi d}{2\gamma \Phi_s} \right)^{3/2} \quad (32)$$

With the monolayer parameters $A = 15.5$ and $B = 3.2$ (cf. Fig. 7) and $\Phi_s = 0.8$, we obtain the crossover in the wet limit: $Ca^{**} \approx 0.02 (\Pi d/\gamma)^{3/2}$. Thus, as indicated in Table 4, for the small bubbles ($d = 82 \mu\text{m}$), the data points lie in the range $Ca \geq Ca^{**}$, whereas for the large bubbles ($d = 115 \mu\text{m}$), the data span above and below the Ca^{**} crossover. This prompts us to plot the shear stress as a function of the quantity $4\Phi_s\gamma(A Ca + B\sqrt{3\Pi d/(2\Phi_s\gamma)} Ca^{2/3})/(\pi d)$. As seen in Fig. 10, the data obtained for both bubble sizes and different osmotic pressures collapse on a master curve with the monolayer parameters A and B . This result shows that the parameter that governs the sliding of foams with mobile interfaces is the ratio Π/P_c . It also shows the range of Ca , depending on Π/P_c , where the linear friction regime is dominant. In practice, it requires very small Π/P_c values or large capillary numbers. Since the foam slips as a plug along the wall, there is no friction due to flow between neighboring bubbles. Therefore, similarly to the monolayer, it exhibits less friction than an isolated bubble. We must keep in mind that the coefficients A and B both depend on the physicochemical constitution of the foaming solution. Indeed, the nature and concentration of surfactant tune: (i) the equilibrium bubble-plane separation distance, which in turn has an impact on A , and (ii) the rigidity of the liquid-gas interfaces that sets the stress boundary condition at the liquid-gas interface and that affects both A and B .

6 Summary and concluding remarks

We have studied the friction of a bubble monolayer and a 3D foam close to the jamming transition as they creep along a smooth solid wall. To investigate the behavior close to this wet

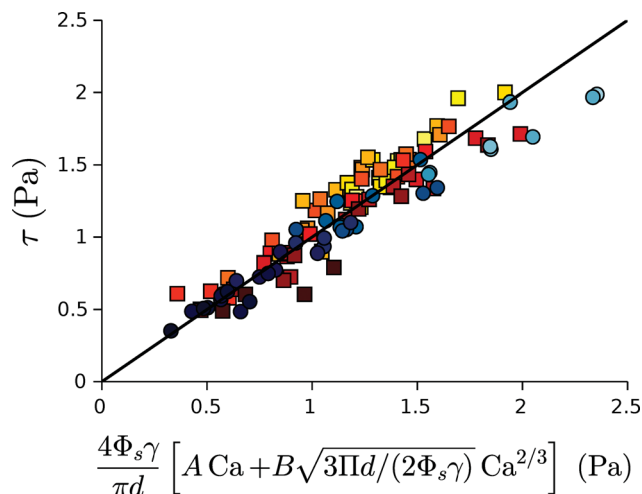


Fig. 10 Wall shear stress τ measured for 3D foams, for the data of Fig. 9a and b (same symbols and legend). The straight line corresponds to eqn (31) with the monolayer parameters $A = 15.5$ and $B = 3.2$ (cf. Fig. 7) and the fraction of the surface area occupied by the bubbles $\Phi_s = 0.8$.

limit, the monolayer or the 3D foam is made to move along an inclined plane immersed in the foaming solution. The bubble velocity is measured by direct visualization. We consider small bubbles with Bond numbers Bo in the range 0.0009–0.5 in the case of monolayers, and low reduced osmotic pressure $\Pi d/\gamma$ in the range 0.006–0.06 for foams. In both cases, we have small bubble velocities *i.e.* capillary numbers Ca in the range 10^{-6} to 10^{-3} . We determine the relation between the force F exerted on a bubble in a monolayer and the capillary number, as well as the relation between the wall shear stress τ and Ca for the 3D foam. We show that, when the bubbles are almost spherical (*i.e.* small Bond number for the monolayer or small reduced osmotic pressure for the foam) the friction force is Stokes-like with $F \propto Ca$ whereas it increases as $V^{2/3}$ in the opposite case. The crossover between the two regimes is set by the characteristic capillary number $Ca^* \sim Bo^{3/2}$ for the monolayer or $Ca^{**} \sim (\Pi d/\gamma)^{3/2}$ for the foam.

Our observations where $F \propto Ca$ are the first evidence for the Stokes-like friction regime that accompanies the creep of bubbles along a wall. The drag force is well described by a lubrication model where the separation distance between the bubble and the wall is set by repulsive long range forces (van der Waals and electrostatic repulsion in our case) counterbalanced by buoyancy. The friction coefficient $\zeta_m = F/V$ of a bubble in a dense monolayer is shown to be smaller than that of an isolated bubble which is intermediate between those expected either for mobile interfaces²⁰ (tangential stress free boundary condition) or rigid interfaces³⁰ (no-slip boundary condition). For the 3D foam, we evidence the linear relationship $\tau \propto Ca$ which is similarly described by a Stokes-like friction at the bubble scale. The contact film thickness is fixed by the balance between the long range forces and the osmotic pressure that presses the bubbles against the wall. Consistently, the prefactor of this relation is equal within 10% to the prefactor deduced from the monolayer friction coefficient ζ_m . A linear friction relation

$F \propto Ca$ has been introduced as a simplified assumption in numerical simulations of 2D foams flowing in Hele-Shaw cells using the viscous froth model.⁸ Our findings show to what extent this assumption is justified in the regime of wet foams.

At small $Ca < Ca^*$, we demonstrate that the monolayer friction is dominated by viscous flow in the dynamic meniscus at the transition region between the contact film and the spherical part of the bubble. We show that $F \propto V^{2/3}$ with a prefactor that is about 2.5 times larger than that expected in the case of mobile interfaces.²⁷ This enhanced drag is consistent with the fact that our surfactant concentration, although superior to the critical micellar concentration, is not large enough to completely remobilize the interfaces.^{32,33} In this situation, surface stress gradients are expected to increase velocity gradients in the dynamic meniscus, which increases the drag. For 3D foams near the jamming transition with $Ca < Ca^*$, the shear wall stress variations with Ca and the reduced osmotic pressure are well described by the relation $\tau \propto \sqrt{\Pi d}/\gamma Ca^{2/3}$. This dependency with Ca is in full agreement with that observed for the monolayers. It is also consistent with that previously found for dry foams.^{9,11}

Furthermore we show that the total drag force exerted on a bubble in a monolayer as well as the total wall shear stress exerted on a 3D foam can be expressed as the sum of a Stokes-like and a Bretherton-like friction term. Remarkably, the prefactors of each term (A and B in eqn (28)) are the same as those of the monolayer drag force (eqn (23)) provided that the impact of the osmotic pressure on the size of the contact film is correctly taken into account. Therefore, eqn (28) predicts the wall shear stress in the whole range of osmotic pressure Π . Using the relationship between Π and the gas volume fraction Φ , established for the full range of Φ , the wall shear stress can thus equivalently be expressed as a function of Φ .

Our model will be useful to predict the wall boundary condition of the velocity profile of foams flowing in any given geometry. By comparing the shear wall stress (eqn (28)) to the bulk foam stress-strain rate constitutive relation,^{2,42} one can predict the flow profile in the full range of gas volume fraction. This will be particularly useful in applications where foams flow through pipes or channels¹⁸ as well as for rheological measurements where wall slip cannot be avoided.

In further work, it will be interesting to study how the prefactors A and B are tuned by the interfacial rigidity, which depends on the chemical properties and the concentration of the surfactants. In the mobile case, one expects both A and B to be affected depending on whether partial or complete surfactant remobilization is achieved. The rigid case can be reached upon addition of a poorly soluble co-surfactant to the foaming solution. It has been shown that in this case wall slip of dry foams is drastically modified compared to the mobile case since the contact film then plays a dominant role in the dissipation.³ Two dissipation mechanisms in the film have been proposed,^{9,13} which lead to different scalings of the wall shear stress with Ca . An investigation of the wall stress as a function of osmotic pressure (or equivalently the gas volume fraction) down to the jamming transition should reveal which mechanism is at play. Further work related to applications could clarify how the pressure drop of wet foams in pipe flows can be minimized.

Previous experiments in this configuration⁴⁷ have evidenced a linear relation between the pressure drop and the flow velocity which is reminiscent of the linear friction that we observe at $Ca \gg Ca^*$.

Finally, we point out two open questions. The first one concerns the slippage against a sticky surface obtained when the foaming solution only partially wets the surface with a non-zero contact angle. The second one concerns the slippage on a rough surface. Empirically, it is known that a surface roughness comparable to the bubble size can prevent wall slip.¹ However the hydrodynamic mechanisms at play have not been investigated. Ultimately, if gas is trapped in the microstructures of the surface forming a bubble mattress, the situation could switch between a slippery one and a sticky one.⁴⁸ This would be of great interest for the flow of foams in confined geometries.

Acknowledgements

We thank D. Qu  r   for stimulating discussions. We gratefully acknowledge financial support from the European Space Agency (Contract MAP AO 99-108) and the Centre National d'Etudes Spatiales (agreement CNES/CNRS no. 127233 and no. 130615). M.L.M. was supported by a postdoctoral fellowship from the Centre National d'Etudes Spatiales.

References

- 1 I. Cantat, S. Cohen-Addad, F. Elias, F. Graner, R. H  hler, O. Pitois, F. Rouyer and A. Saint-Jalmes, *Foams: Structure and Dynamics*, Oxford University Press, Oxford, 2013.
- 2 S. Cohen-Addad, R. H  hler and O. Pitois, *Annu. Rev. Fluid Mech.*, 2013, **45**, 241–267.
- 3 N. D. Denkov, S. Tcholakova, K. Golemanov, K. P. Ananthpadmanabhan and A. Lips, *Soft Matter*, 2009, **5**, 3389–3408.
- 4 B. Herzhaft, S. Kakadjian and M. Moan, *Colloids Surf., A*, 2005, **263**, 153–164.
- 5 S. P. Meeker, R. T. Bonnecaze and M. Cloitre, *Phys. Rev. Lett.*, 2004, **92**, 198302.
- 6 J. R. Seth, C. Locatelli-Champagne, F. Monti, R. T. Bonnecaze and M. Cloitre, *Soft Matter*, 2012, **8**, 140–148.
- 7 N. Kern, D. Weaire, A. Martin, S. Hutzler and S. J. Cox, *Phys. Rev. E: Stat., Nonlinear, Soft Matter Phys.*, 2004, **70**, 041411.
- 8 S. J. Cox, *Colloids Surf., A*, 2005, **263**, 81–89.
- 9 N. D. Denkov, V. Subramanian, D. Gurovich and A. Lips, *Colloids Surf., A*, 2005, **263**, 129–145.
- 10 N. D. Denkov, S. Tcholakova, K. Golemanov, V. Subramanian and A. Lips, *Colloids Surf., A*, 2006, **282**, 329–347.
- 11 S. Marze, D. Langevin and A. Saint-Jalmes, *J. Rheol.*, 2008, **52**, 1091–1111.
- 12 B. Embley and P. Grassia, *Colloids Surf., A*, 2011, **382**, 8–17.
- 13 I. Cantat, *Phys. Fluids*, 2013, **25**, 031303.
- 14 H. Princen, *Langmuir*, 1986, **2**, 519–524.
- 15 R. H  hler, Y. Yip Cheung Sang, E. Lorenceau and S. Cohen-Addad, *Langmuir*, 2008, **24**, 418–425.
- 16 W. Drenckhan, S. J. Cox, G. Delaney, H. Holste, D. Weaire and N. Kern, *Colloids Surf., A*, 2005, **263**, 52–64.

- 17 P. Marmottant and J.-P. Raven, *Soft Matter*, 2009, **5**, 3385–3388.
- 18 P. Stevenson, *Foam Engineering: Fundamentals and Applications*, J. Wiley, 2012.
- 19 J. R. Seth, M. Cloitre and R. T. Bonnecaze, *J. Rheol.*, 2008, **52**, 1241–1268.
- 20 L. R. White and S. L. Carnie, *J. Fluid Mech.*, 2012, **696**, 345–373.
- 21 L. A. del Castillo, S. Ohnishi, L. R. White, S. L. Carnie and R. G. Horn, *J. Colloid Interface Sci.*, 2011, **364**, 505–511.
- 22 F. Bretherton, *J. Fluid Mech.*, 1961, **10**, 166–188.
- 23 B. Dollet and I. Cantat, *J. Fluid Mech.*, 2010, **652**, 529–539.
- 24 I. Cantat, N. Kern and R. Delannay, *Europhys. Lett.*, 2004, **65**, 726–732.
- 25 E. Terriac, J. Etrillard and I. Cantat, *Europhys. Lett.*, 2006, **74**, 909–915.
- 26 P. Aussillous and D. Quéré, *Europhys. Lett.*, 2002, **59**, 370–376.
- 27 S. R. Hodges, O. E. Jensen and J. M. Rallison, *J. Fluid Mech.*, 2004, **512**, 95–131.
- 28 L. Mahadevan and Y. Pomeau, *Phys. Fluids*, 1999, **11**, 2449–2453.
- 29 J. Israelachvili, *Intermolecular and Surfaces Forces*, Academic Press, London, 1992.
- 30 M. Chaoui and F. Feuillebois, *Q. J. Mech. Appl. Math.*, 2003, **56**, 381–410.
- 31 D. Langevin, *Annu. Rev. Fluid Mech.*, 2014, **46**, 47–65.
- 32 O. Ou Ramdane and D. Quéré, *Langmuir*, 1997, **13**, 2911–2916.
- 33 B. Scheid, J. Delacotte, B. Dollet, E. Rio, F. Restagno, E. van Nierop, I. Cantat, D. Langevin and H. Stone, *Europhys. Lett.*, 2010, **90**, 24002.
- 34 G. Batchelor, *An Introduction to Fluid Dynamics*, Cambridge University Press, 1967.
- 35 A. Saugey, W. Drenckhan and D. Weaire, *Phys. Fluids*, 2006, **18**, 053101.
- 36 A. Maestro, W. Drenckhan, E. Rio and R. Höhler, *Soft Matter*, 2013, **9**, 2531–2540.
- 37 The ratio Π/P_c is equal to the function $f(\Phi)$ defined by eqn (12) in ref. 14. Thus, we have $f(\Phi) = \Phi_s \ell^2 / d^2$.
- 38 T. G. Mason, M.-D. Lacasse, G. S. Grest, D. Levine, J. Bibette and D. A. Weitz, *Phys. Rev. E: Stat. Phys., Plasmas, Fluids, Relat. Interdiscip. Top.*, 1997, **56**, 3150.
- 39 M. van Hecke, *J. Phys.: Condens. Matter*, 2010, **22**, 033101.
- 40 A.-L. Biance, S. Cohen-Addad and R. Höhler, *Soft Matter*, 2009, **5**, 4672–4679.
- 41 E. Lorenceau, Y. Yip Cheung Sang, R. Höhler and S. Cohen-Addad, *Phys. Fluids*, 2006, **18**, 097103.
- 42 R. Lespiat, S. Cohen-Addad and R. Höhler, *Phys. Rev. Lett.*, 2011, **106**, 148302.
- 43 S. P. L. Marze, A. Saint-Jalmes and D. Langevin, *Colloids Surf., A*, 2005, **263**, 121–128.
- 44 R. Lespiat, PhD thesis, Université Paris-Est, 2009.
- 45 C.-W. Park, *J. Colloid Interface Sci.*, 1991, **146**, 382–394.
- 46 J. Ratulowski and H. C. Chang, *J. Fluid Mech.*, 1990, **210**, 303–328.
- 47 M. Briceño and D. Joseph, *Int. J. Multiphase Flow*, 2003, **29**, 1817–1831.
- 48 A. Steinberger, C. Cottin-Bizonne, P. Kleimann and E. Charlaix, *Nat. Mater.*, 2007, **6**, 665–668.